Low-velocity impact cratering experiments in a wet sand target

Haruna Takita and Ikuro Sumita*

Division of Earth and Environmental Sciences, Graduate School of Natural Science and Technology, Kanazawa University, Kanazawa, 920-1192, Japan

(Received 29 April 2013; published 26 August 2013)

Low-velocity impact cratering experiments were conducted in a wet sand target. With the addition of interstitial water, the sand stiffens and the yield stress σ_y increases by a factor of 10 and we observe a significant change in the resulting crater shape. A small water saturation ($S \sim 0.02$) is sufficient to inhibit the crater wall collapse, which causes the crater diameter d to decrease and the crater depth to increase, and results in the steepening of the crater wall. With a further addition of water ($S \sim 0.04$), the collapse is completely inhibited such that cylindrical craters form and the impactor penetration depth δ and ejecta dispersal are suppressed. However, for $S > 0.7$, the wet sand becomes fluidized such that both d and δ increase thereafter. Comparing the relevant stresses, we find that cylindrical craters form when the yield stress is more than about three times larger than the gravitational stress such that it can withstand collapse. Experiments with different impactor sizes D and velocities indicate that for $S \leqslant 0.02$, gravity-regime scaling applies for d. However, the scaling gradually fails as S increases. In contrast, we find that δ/D can be scaled by the inertial stress normalized by the yield stress, for a wide range of S. This difference in the scaling is interpreted as arising from d being affected by whether or not the crater wall collapses, whereas δ is determined by the penetration process that occurs prior to collapse. The experimental parameter space in terms of dimensionless numbers indicates that our experiments may correspond to impact cratering in small asteroids.

DOI: 10.1103/PhysRevE.88.022203 PACS number(s): 45.70.−n, 47.57.Gc, 96.12.ke, 96.25.Pq

I. INTRODUCTION

It is well known that the interstitial liquid in granular matter such as sand acts as a cohesive force to make it stiffen, allowing us to build, e.g., sand castles. The physics of wet granular matter has attracted much attention [1,2]. For example, the effect of the liquid on the stability angle of a granular pile has been intensively studied [3–5]. Impact cratering into a wet granular matter can also provide insight into its peculiar properties. Motivated by features suggesting fluidized flow in Martian craters, experiments on a fully saturated granular matter have been conducted [6,7]. Wet granular matter has also been used to study crater scaling laws (see [8] and references therein). Recently, low-velocity impact experiments in wet granular matter have been pursued [9,10]. Manga *et al.* [9] measured the penetration depth into wet (mostly water-saturated) sand as a function of impact velocity. However, the water saturation S in the wet sand was not measured or systematically varied. Marston *et al.* [10] varied S and investigated how the impactor penetration depth varies with S, but the detailed changes of the crater shapes were not studied. Here we report a series of experiments that investigate how the crater shape changes with water saturation. We study how the craters form, classify their shapes, and measure their characteristic length scales. In addition, we vary the impactor size and its impact velocity to constrain how the crater length scales can be scaled using a combination of changeable parameters.

II. PHYSICAL PROPERTIES OF WET SAND

We use well-sorted beach sand (Chirihama, Japan), with a diameter of 0.204 ± 0.002 mm (measured by Shimadzu, SALD-2200J and confirmed by a microscope) and a density of $\rho_s = 2610$ kg/m^3. The angle of repose of the sand pile is $\theta_r \simeq 37^\circ$ (friction coefficient $\mu = 0.75$), which is identical to the documented value [11]. This angle is larger than the $\theta_r \sim 22^\circ$–24° for spherical glass beads [10,12] and the difference seems to arise from the shape of the particles [11].

We characterize the wet sand using the volumetric packing fraction ϕ of the sand particles and the volumetric fraction of water saturation S within the void space. Accordingly, the wet sand (target) density becomes $\rho_t = \phi\rho_s + S(1-\phi)\rho_w$, where ρ_w is the density of water. In our impact cratering experiments, we took particular care to maintain ϕ within the range of $0.49 < \phi < 0.54$ with an average of $\phi = 0.52 \pm 0.01$ (with an error that is the standard deviation). We vary S in the range of $0 \leqslant S \leqslant 0.789$. The value of ϕ of the wet and dry sand used in our experiments is smaller than the value for dense random close packing of spheres ~0.64 [13]. This is because the wet sand is stiff and resists deformation such that ϕ becomes small; ϕ of the dry sand is also smaller than ~0.64 because we fill the container loosely in order to match ϕ of the wet sand. When we fill the container with dry sand and tap it afterwards, the packing fraction becomes $\phi \sim 0.61$. We also measured how θ_r changes with S. We find that $\theta_r \sim 38^\circ$ ($\mu \sim 0.78$) at $S \sim 0.04$, which increases to $\theta_r \sim 46^\circ$ ($\mu \sim 1.0$) at $S \sim 0.12$. Such an increase of θ_r is consistent with that reported previously (see, e.g., [14]).

The wet sand is prepared by spraying a known mass of water on the dry sand and thoroughly mixing it by hand. We check the water content using a portable soil water content meter (DM-18 Takemura Electric Works, Japan), which measures the electrical conductivity. We dry the wet sand in a microwave oven and obtain the mass fraction of water and sand, from which we calculate the water saturation S.

We measure the rheology of the wet sand using a rotating viscometer (Brookfield DVII + PRO 2HB) to which a vane

*isumita@staff.kanazawa-u.ac.jp

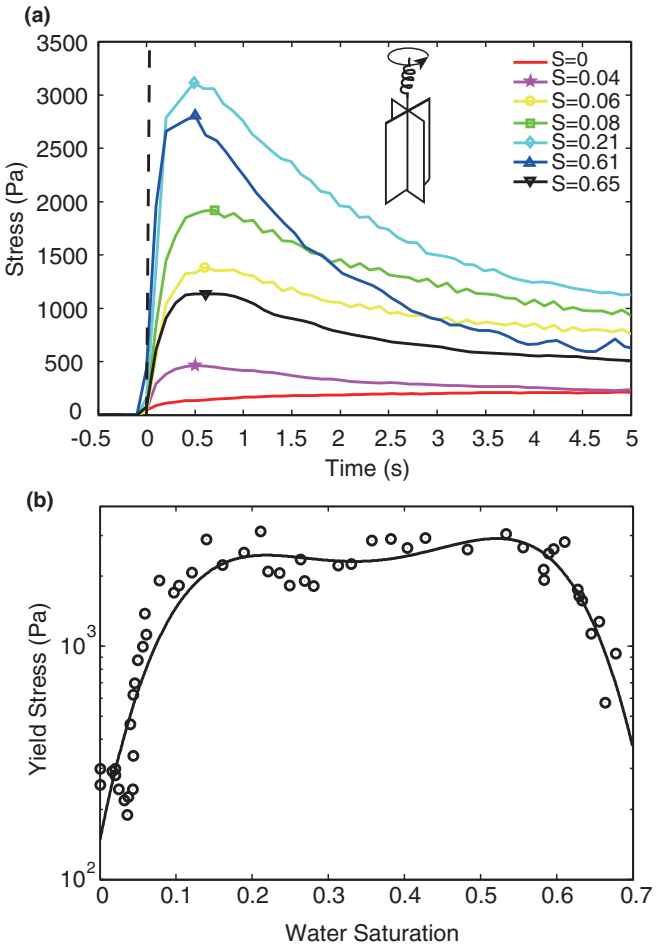

FIG. 1. (Color online) Shear rheology of wet sand. (a) Examples of the stress–time-series data of wet sand with different values of S (with a $\phi = 0.528 \pm 0.006$ error given by standard deviation). The sample was sheared by a viscometer rotating at 100 rpm, to which a vane spindle is attached (see the inset). Yield stresses (maximum stress) for each data are indicated by the corresponding markers. The maximum stress for $S = 0$ is not shown ($\sigma_{y0} = 254$ Pa at $t = 34$ s). The dashed line indicates the spring wind up line corresponding to the case in which the sample does not deform. (b) Yield stress σ_{y0} as a function of S. The packing fraction of all data is $\phi = 0.530 \pm 0.007$. The curve is a fourth-order polynomial fit to $\ln(\sigma_{y0})$ as a function of S in the range of $0 \leqslant S \leqslant 0.68$.

spindle (V74 with a diameter of 5.89 mm and height of 11.76 mm) is attached [see inset of Fig. 1(a)] [15–17]. The height of the vane spindle is comparable to the typical penetration depth of the impactor [Fig. 9(a)]. Here we fill a cylindrical container (diameter 30 mm, height 62 mm) with the wet sand and insert the vane spindle at the center such that its upper end coincides with the wet sand surface. We shear the sample under a rotation rate of 100 rpm, which is the fastest rate that can be imposed using the viscometer. This shear rate corresponds to a shear rate of 2.6 (1/s) if we assume that the whole sample deforms. In comparison, the shear rate during impact cratering can be estimated from $\sim 2v/D$, where v is the impact velocity and D is the impactor diameter, from which we obtain 110–1150 (1/s), which is 40–440 times larger than the shear rate of the rheology measurement.

Examples of the stress–time-series data for wet sand with different values of S are shown in Fig. 1(a). We measure the stress at a sampling frequency of 10 Hz and define time zero when the stress first exceeds 17 Pa, which corresponds to the resolution of the viscometer. Here we also show for reference a spring wind up line, which corresponds to the case in which the sample does not deform. Maximum stresses are indicated by the different markers. The stress–time-series data for the dry sand ($S = 0$) indicate that the stress increases gradually with time up to ~300 Pa. In contrast, when the water saturation exceeds $S \sim 0.04$, we find that the wet sand yields at a peak stress, which we define as the yield stress σ_{y0}. Here a subscript 0 is used to denote that it is the depth-averaged value of the inserted vane spindle. We also find that for $S > 0.04$, the yield stress increases precipitously with S to around $\sigma_{y0} \sim 3000$ Pa, which is about 10 times larger than the stress needed to deform dry sand. Such acute sensitivity of the yield stress to small values of S is consistent with previous works [4,5]. We compare σ_{y0} with the cohesive stress [11], which can be estimated from $\sim \gamma/r = 730$ Pa, where $\gamma \sim 7.3 \times 10^{-2}$ N/m is the air-water surface tension coefficient and $r = 0.1$ mm is the particle radius. Cohesive stress being larger than the stress needed to deform dry sand confirms that the particle size is small enough such that cohesion is important in our experiments. We also note that the initial slope of the stress–time-series data corresponds to the rigidity [15]. Figure 1(a) shows that the wet sand is stiffer than the dry sand.

When the water saturation exceeds $S \sim 0.6$, the yield stress decreases. We plot σ_{y0} as a function of S in Fig. 1(b). Such a dependence of σ_{y0} on S is consistent with results obtained from previous works (see [2] for a review). As noted above, the shear rate of our rheology measurements do not match those of our impact cratering experiments. Accordingly, our using the same values of σ_{y0} to impact the cratering process rests on the assumption that the rate dependence is small. However, σ_{y0} of the same wet sand measured at a shear rate that is smaller by three orders of magnitude (2.6×10^{-3} 1/s) [17] is comparable to that at 2.6 (1/s) within a factor of ~2. This suggests that the shear rate dependence may be small.

We may estimate the effective friction coefficient $\mu_{\rm eff}$ using σ_{y0}. For dry sand, we may estimate $\mu_{\rm eff} = \sigma_{y0}/\rho_t g z \sim 4$, where z is the depth scale where we used the mid-depth of the inserted spindle. This value of $\mu_{\rm eff}$ is larger than $\mu = 0.75$, which is obtained from the angle of repose. Similarly, for the wet sand, we obtain $\mu_{\rm eff} \sim 40$.

III. IMPACT CRATERING EXPERIMENTS

A. Methods

We fill a cylindrical acrylic container (diameter 180 mm, height 90 mm) with wet sand and use a ruler to form a flat surface. This diameter is at least eight times larger than the diameter of the impactor (sphere). In our experiments, the impactor stops at a distance more than 18 mm away from the bottom of the container. Previous work [18] suggests that these width and depth scales of the container are sufficiently large such that the effects of the container walls and the base to the penetration depths become negligible.

For an impactor, we use a stainless steel (SUS440C) sphere (sphericity 0.7 μm) with a density of $\rho_i = 7700 \text{kg/m}^3$. We

use spheres with seven different diameters D in the range of 10.0–22.2 mm, which correspond to varying the impactor mass by a factor of 11. The impactor is dropped using an electromagnet from a fixed height h above the surface of the granular target. The drop height h is the distance between the bottom of the impactor and the target surface, which is varied in the range of $h = 78$–1690 mm corresponding to an impact velocity of $v = 1.2$–5.8 m/s. We use a line laser displacement sensor (Omron ZG2-WDS70, resolution ∼0.1 mm) to measure the surface topography of a line passing through the crater center, before and after the impact. In order to avoid scattering of the laser from the sphere for the case in which it does not fully submerge in the sand, we coated the impactor with a paint. When the impactor is completely submerged in the sand, we use a ruler to measure the penetration depth δ, which is the distance between the original surface and the bottom end of the penetrated impactor, to a resolution of 0.5 mm.

The whole process of impact cratering is recorded using a high speed camera (DITECT HAS-500 or IDT Motion Scope M) at a frame rate of 1000 frames/s. The digitized surface topography is analyzed using MATLAB, from which we determine the surface diameter, crater depth, penetration depth, rim diameter, and rim height.

B. Dimensionless numbers and parameter space

Scalings of crater size have been conventionally made using dimensionless numbers (see, e.g., [8]). We similarly evaluate our experimental parameter space using dimensionless numbers. Here the relevant stress scales are the gravitational stress $\rho_t g D$ for a crater with a depth scale comparable to the impactor size D, the inertial stress of the impactor $\rho_i v^2$, and the yield stress of the target σ_{y0}. Here ρ_t and ρ_i are the density of the target and impactor, respectively, g is the gravitational acceleration, and v is the impact velocity.

We nondimensionalize these stress scales by σ_{y0} to obtain a dimensionless gravity

$$g' = \frac{\rho_t g D}{\sigma_{y0}} = \frac{\pi_2 \pi_4}{\pi_3} \tag{1}$$

and a dimensionless inertia

$$i' = \frac{\rho_i v^2}{\sigma_{y0}} = \frac{1}{\pi_3}. \tag{2}$$

Here g' indicates the resistance of the target material to gravitational collapse. For $g' \gg 1$ the target cannot withstand collapse (gravity regime) and vice versa for $g' \ll 1$ (strength regime). i' indicates the fragility to impact cratering. For $i' \gg 1$, the target is sufficiently fragile for cratering to occur and vice versa for $i' \ll 1$. g' and i' can be related to the traditionally used $\pi_2 = gD/v^2$, $\pi_3 = \sigma_{y0}/\rho_i v^2$, and $\pi_4 = \rho_t/\rho_i$ [8], as shown in Eqs. (1) and (2). We remark that we only use the yield stress σ_{y0} to characterize the target rheology and other properties such as viscoelasticity are not included. Accordingly, Eqs. (1) and (2) are insufficient to characterize the crater features in which viscoelasticity is relevant.

Here we calculate g' and i' for our experiments in the range of $0 \leqslant S < 0.6$, which covers the simple, transitional, and cylindrical craters whose features are described in detail in the next section. For σ_{y0} we use a function obtained by fitting the data in Fig. 1(b) (see the caption for details).

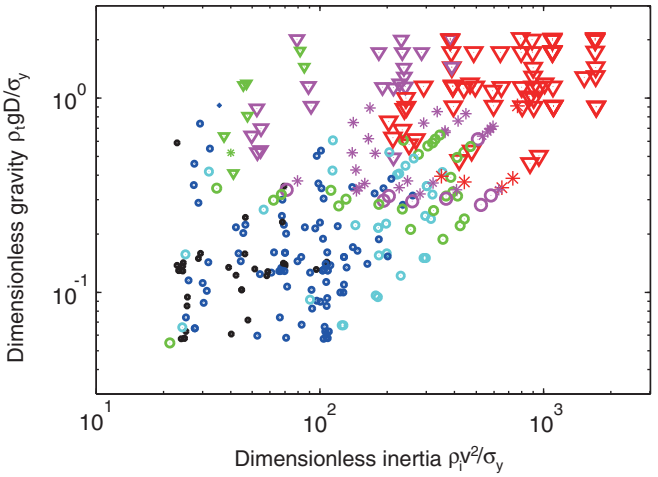

FIG. 2. (Color online) Experimental parameter space and the resulting crater surface diameters and shapes for cases in which $S < 0.6$ (a total of 320 experiments, where $\phi = 0.518 \pm 0.010$). Dimensionless gravity g' and dimensionless inertia i' are given by Eqs. (1) and (2), respectively. Here the marker colors (and sizes) indicate the dimensionless crater diameter $d' = d/D$ in ranges of 0.9–1.0 (black, smallest marker), 1.0–1.1 (blue), 1.1–1.2 (light blue), 1.2–1.5 (green), 1.5–2.5 (purple), and 2.5–5.0 (red, largest marker). Marker shapes correspond to the different crater shapes, which are shown in Fig. 3: inverted triangles, simple; asterisks, transitional; and circles, cylindrical.

In Fig. 2 we plot our experiments in the i'-g' parameter space. Here we plot experiments in the range of $S < 0.6$ (a total of 320), excluding those for $S \geqslant 0.6$ in which the yield stress decreases with S. We find that our experiments are conducted at $20 < i' < 2000$ and $0.05 < g' < 2$. Our range of g' covers $g' \sim 1$, from which we expect that our experiments using a wet sand target can reveal the transition between the gravity and strength regimes. Indeed, previous explosive experiments using alluvial soil in a centrifuge have shown that the transition occurs for $0.1 < g' < 10$ [8,19], which partially overlaps our experimental range. We also note that despite the low velocity of our experiments, $i' \gg 1$, indicating that the inertial stress is large enough compared to the yield stress that impact craters can form. For comparison we evaluate the same dimensionless numbers for the recent impact cratering experiments using snow and rock targets in the strength regime. Experiments using snow at impact velocities of $v = 31$–150 m/s [20] are at $g' \sim 10^{-5}$–10^{-4} and $i' \sim 10$–300, whereas those using sedimentary rock at $v = 800$–6900 m/s [21] are at $g' \sim (5 \times 10^{-6})$–$(5 \times 10^{-5})$ and $i' = 200$–10^5. A smaller g' value for these experiments confirms that these experiments are in the regime in which the target strength is more important than in our experiments.

C. Crater shape diversity

Figure 3 shows how the shapes of the impact craters change as water saturation S increases, for a fixed impactor size

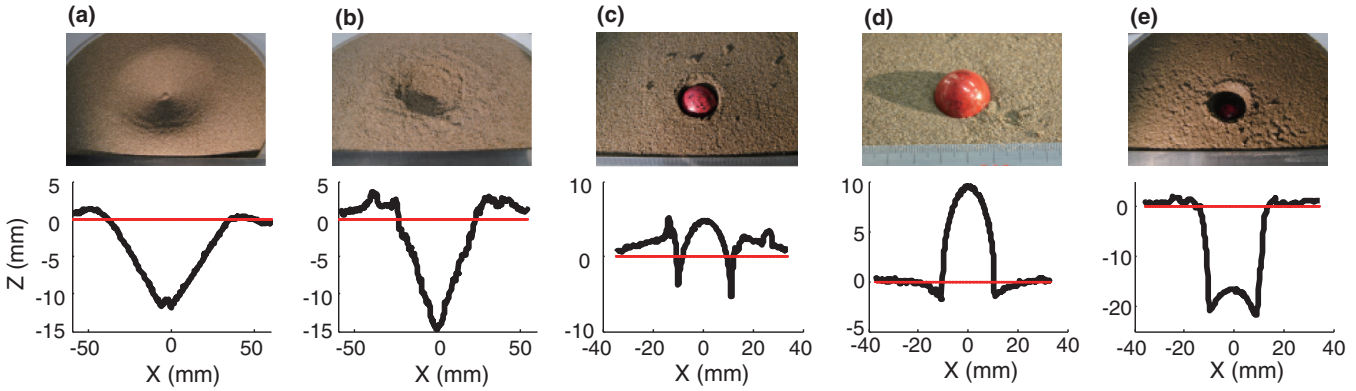

FIG. 3. (Color online) Five types of crater shapes observed in our experiments as a function of water saturation S of the wet sand. Photographs and corresponding surface topographies (X and Z are horizontal and vertical dimensions, respectively, in mm) are shown. Here the impactor diameter is $D = 22.2$ mm and the release height is $h = 1678$ mm. A red horizontal line at height zero indicates the target surface prior to impact. The packing fraction is $\phi = 0.518 \pm 0.012$. (a) A simple crater for $S = 0$ with a central peak formed from the ascending granular jet (see movie 1 in [22]). (b) Transitional crater for $S = 0.034$ with a corrugated wall (see movie 1 in [22]). (c) Cylindrical crater for $S = 0.190$ and an exposed impactor (see movie 2 in [22]). (d) Cylindrical crater for $S = 0.649$ with a depression at the rim and an exposed impactor (see movie 2 in [22]). (e) Spattered crater for $S = 0.686$ (see movie 2 in [22]).

$D = 22.2$ mm and a release height $h = 1678$ mm. Here we define five types, which are described in detail below.

Figure 3(a) shows a simple crater at $S = 0$, characterized by a conical shape. The crater has a crater depth to surface diameter ratio approximately equal to 0.16, which results in the angle of the crater wall slope of $\sim 17^\circ$, an angle that is about half the angle of repose ($\simeq 37^\circ$). Here the crater depth is the depth from the original surface and the surface diameter is the diameter defined from the intersection with the original surface. We can confirm the three stages of crater formation (see movie 1 in [22]): the impact, penetration, and collapse of the crater wall (see, e.g., [23]). Importantly, the wall collapse causes the crater diameter to enlarge and the depth to become shallower. In addition, for a dry sand target, when the impactor energy exceeds $\simeq 0.2$ J, a vertical granular jet ascends from the center of the crater (see, e.g., [24]) and a central peak forms, which is evident in Fig. 3(a). With a small addition of water, the rim becomes higher. This can be interpreted as a consequence of the suppression of the collapse that acts to destroy the rim. Such simple craters were found to form for $0 \leqslant S < 0.022$.

Figure 3(b) shows a crater at $S = 0.034$, which we call a transitional crater between the simple crater at $S < 0.022$ and a cylindrical crater at $S > 0.038$. Here the crater wall becomes corrugated and can be distinguished from a simple crater by the crater wall no longer having a smooth surface. This crater has a smaller diameter and a deeper depth, and hence a steeper slope, as compared to Fig. 3(a). This can be understood from wet sand becoming stiffer and more resistant to collapse. When the collapse is inhibited, the enlargement of the crater diameter is suppressed and the crater becomes deeper. As noted above, the crater rim becomes higher. We also find that ejecta form larger blocks (see movie 1 in [22]) [9]. Such a transitional crater was found to form for $0.022 < S < 0.038$.

Figure 3(c) shows a crater at $S = 0.190$, which we call a cylindrical crater (see movie 2 in [22]). Here the wet sand becomes sufficiently stiff that wall collapse no longer occurs. In other words, the crater formation consists only of the impact and penetration stages. Limited ejecta dispersal occurs in the form of blocks and the rim height becomes lower [Fig. 6(c)]. A cylindrical crater formed for $0.038 < S < 0.50$. The critical value of S for cylindrical craters to form is close to $S \sim 0.04$. This value coincides with the S value above which the yielding occurs and σ_y increases precipitously (Fig. 1). Such cylindrical craters formed by deforming the target and are characteristic of our low-velocity impact experiments.

Figure 3(d) shows a crater at $S = 0.649$, which is a particular example of a cylindrical crater and is characterized by a depression in the circumference of the crater, indicating a viscous deformation of wet sand (see movie 2 in [22]). Such a cylindrical crater with a depression formed for $0.500 < S < 0.668$. Note that for this case, apart from the depression, the crater shape is determined by the shape of the impactor.

Figure 3(e) shows a crater at $S = 0.686$. Here the wet sand becomes sufficiently fluidized that the crater diameter and depth increase (see movie 2 in [22]). Such a crater formed for $0.668 < S < 0.764$, which we call a spattered crater. Ejecta dispersal revived and the rim became higher again [Fig. 6(c)]. We also observed that the wet sand surface dilated upon impact, but then subsided soon afterwards, indicating an elastic response (see movie 2 in [22]).

Images during crater formation viewed from the top and from the side are shown in Figs. 4(a)–4(c) and Figs. 5(a)–5(d), respectively (see also movies 1–3 in [22]). The images show that as S increases from $S = 0$ to 0.04, the ejecta form blocks. A drastic suppression of ejecta dispersal at $S = 0.18$ [Fig. 5(c)] and spattering of fluidized ejecta at $S = 0.76$ [Fig. 5(d)] are also evident.

In Figs. 6(a)–6(c) we show the surface diameter, penetration depth, and rim height nondimensionalized by the impactor diameter, as a function of water saturation S, for $D = 22.2$ mm and $h = 1678 \pm 2$mm. Here the rim height is measured as follows. When a peak rim height can be identified, we use the average of the two rim heights obtained from the topography. For a cylindrical crater with a depression, such peak heights cannot be identified. Accordingly, we define the rim height as the depth at which the topography deviates from

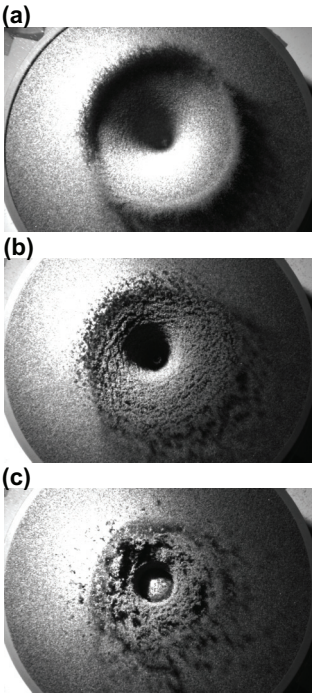

FIG. 4. (Color online) Images during impact cratering observed from the top at $t = 0.054$ s after the impact ($D = 22.2$ mm and $h = 1678$ mm). Results for targets with different S are shown. The widths of the images are 180 mm. (a) Simple crater for $S = 0$ and $\phi = 0.528$ (see movie 1 in [22]). (b) Transitional crater for $S = 0.034$ and $\phi = 0.527$ (see movie 1 in [22]). (c) Cylindrical crater for $S = 0.042$ and $\phi = 0.524$ (see movie 1 in [22]).

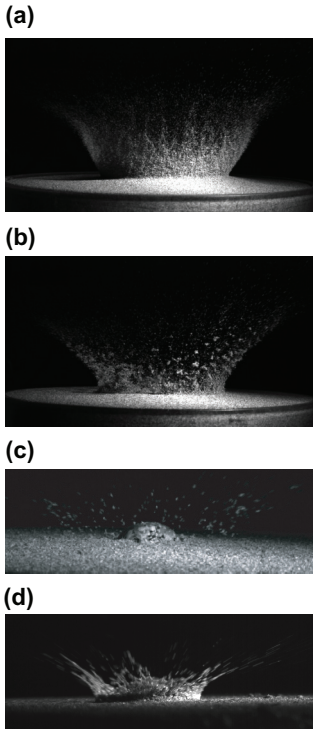

FIG. 5. (Color online) Images during impact cratering observed from the side ($D = 22.2$ mm and $h = 1078$ mm). Results for targets with different S are shown. The time of the impact is $t = 0$. The widths of the images are (a) and (b) 180 mm and (c) and (d) 90 mm. (a) Simple crater for $S = 0$ ($\phi = 0.528$) at $t = 0.056$ s (see movie 3 in [22]). (b) Cylindrical crater for $S = 0.042$ ($\phi = 0.527$) at $t = 0.056$ s (see movie 3 in [22]). (c) Cylindrical crater for $S = 0.184$ ($\phi = 0.517$) at $t = 0.019$ s (see movie 3 in [22]). (d) Spattered crater for $S = 0.756$ ($\phi = 0.518$) at $t = 0.004$ s (see movie 3 in [22]).

a cylindrical profile and the rim height becomes a negative value. Figures 6(a) and 6(b) show the S dependence that is anticorrelated with the S dependence of the yield stress [Fig. 1(a)]. Figure 6(c) shows that a maximum rim height forms at around $S \simeq 0.04$, which we interpret as a combined result of the suppression of wall collapse at smaller S and the suppression of ejecta dispersal at larger S. For this value of h, the impactor is submerged in the target for $S < 0.039$. In Fig. 6(d) we plot the crater depth to surface diameter ratio for the craters in this S range. For dry sand ($S = 0$), this ratio is $\sim$0.16 and slightly decreases with impact energy [Fig. 8(b)]. The ratio increases for $S > 0.02$, which is a combined result of the increase of crater depth [Fig. 8(a)] and the decrease of surface diameter [Fig. 6(a)]. The increase of this ratio with target strength is consistent with the compiled results for dry sand, ice, and snow targets [20] at faster impact velocities of the order of 10–100 m/s.

We have conducted a total of 340 experiments with different combinations of impactor diameter D and release heights h. We select experiments in the range of $S < 0.60$ (a total of 320), which we plot in Fig. 2 in the parameter space of dimensionless inertia i' and dimensionless gravity g'. In this plot we classify the craters according to the magnitude of the dimensionless surface diameter d' (which is equal to the ratio of the surface diameter to the impactor diameter) using the marker colors (and sizes) and the crater shape by the marker shapes. The plot shows that there is a general trend of d' becoming larger with i' and g', i.e., as the inertia and gravity becomes larger compared to the yield stress. In contrast, in our experimental range, the crater shape is determined primarily by g'. For $g' < 0.4$, only cylindrical craters form.

The critical S, which separates the different crater shapes, may depend on h, and hence on the impact velocity, as well as on the impactor diameter D. In our experimental range, we find a slight increase of the critical S separating the transitional and cylindrical craters with h; otherwise no dependence was found. In detail, we find that the critical S increased from $S \simeq 0.028$ at $h = 90$ mm to $S \simeq 0.037$ at $h = 1690$ mm.

D. Scaling relations

We now consider how the crater dimensions scale with the experimental parameters. First we consider the crater diameter. We choose to use the surface diameter rather than the rim diameter because for some cases the crater rim cannot be identified. Figure 7(a) shows the relation between the surface diameter d (mm) and the impact energy $E = mgh$ (J) for different ranges of S. Here, in order to vary E, we change m (impactor mass) and release heights h. We fit the data for a dry sand target ($S = 0$) using a power-law relation to obtain $d = 87.5E^{0.271\pm0.007}$ (using a rim diameter $d = 105.6E^{0.265\pm0.006}$). The plot shows that the data for different impactor mass collapse if they have the same impact energy. The exponent is close to but slightly larger than 0.25, which is the value for

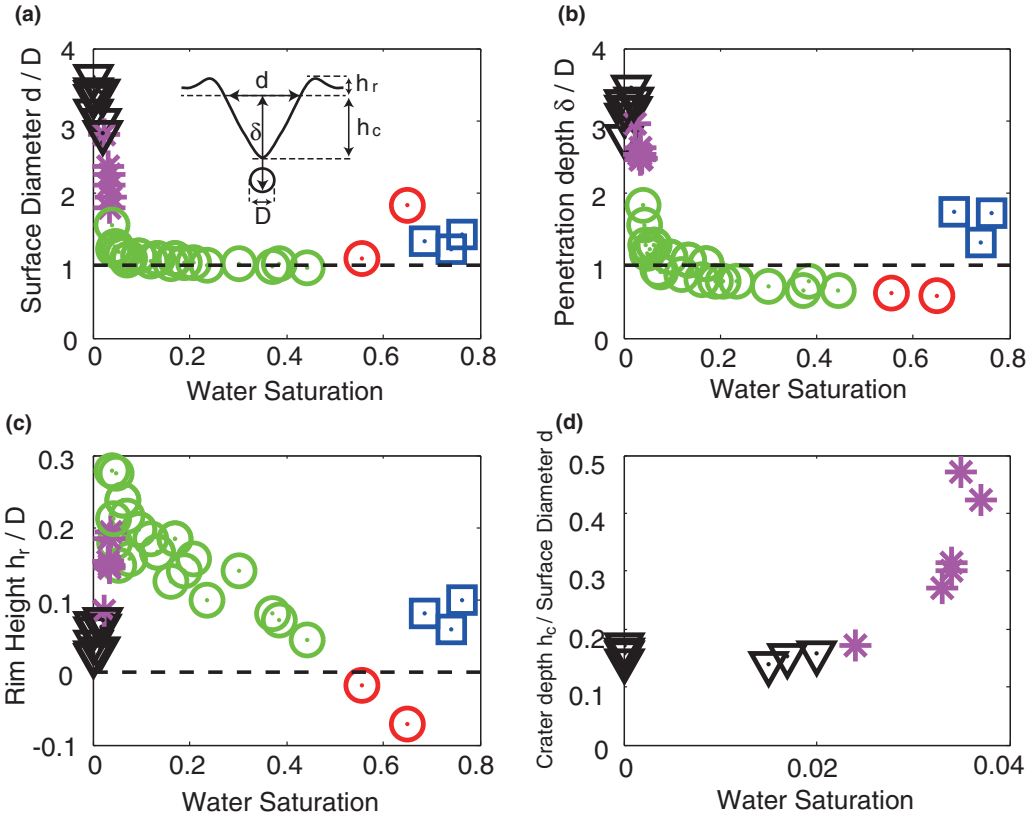

FIG. 6. (Color online) Water saturation S dependence of the length scales characterizing the crater for $D = 22.2$ mm and $h = 1678$ mm (impact energy $E = 0.73$ J): (a) d/D, with d the surface diameter and D the impactor diameter (the inset shows the definition of the scales); (b) δ/D, with δ the penetration depth; (c) h_r/D, with h_r the rim height; and (d) h_c/d, with h_c the crater depth. The marker shapes (and colors) indicate the crater shapes: inverted triangles, simple; asterisks, transitional; circles [green (light gray)], cylindrical; circles [red (dark gray)], cylindrical with circumferential depression; and squares, spattered. The impactor is fully submerged in the target for the simple and transitional craters. The packing fraction of the target is $\phi = 0.519 \pm 0.010$.

the scaling law in the gravity regime [8]. For the transitional craters, we obtain a power-law relation of $d = 55.0E^{0.251\pm0.008}$ (using a rim diameter $d = 77.1E^{0.250\pm0.008}$), with an exponent value that agrees better with 0.25. For the cylindrical craters, the diameter becomes comparable to the impactor size D and as a result, for a given E, the diameter data vary with D [see Fig. 7(a)] and the same scaling no longer applies. Here we plot the data for cylindrical craters with different colors (linewidths) according to the S range. In Fig. 7(b) we replot the data for the cylindrical craters by normalizing the surface diameter d by the impactor diameter D. We find that there is a trend of d/D approaching $\sim$1.0 as S increases.

In Fig. 8(a) we plot the crater depth as a function of impact energy for the cases in which the impactor is fully submerged in the target. Here we consider the simple and transitional craters because for most of these cases the impactor is fully submerged. The plot shows that the crater depths of the transitional craters are slightly deeper than those of the simple craters, which can be interpreted as a consequence of the inhibition of crater wall collapse. The power-law exponents for the simple and transitional craters are similar ($\sim$0.20) and are smaller than the power-law exponent 0.25 for the diameter-energy scaling [Fig. 7(a)]. Crater depths of the transitional craters have a larger data scatter compared to the simple craters. This is because in the range of $0.02 < S < 0.04$, which covers the transitional craters, the crater depth is sensitive to a slight change of S. In Fig. 8(b) we plot the ratio of crater depth to surface diameter, which is proportional to the slope of the crater wall. The plot shows that the transitional craters have a larger ratio (i.e., a steeper slope). We also find that for simple craters, the ratio becomes smaller with the impact energy, which is a consequence of the different power-law exponents of diameter and depth to impact energy. This result is also consistent with previous work [24].

Next we consider the penetration depth δ. Here we note that δ is larger than the crater depth when the impactor is fully submerged in the target. Following previous works [10,12,18,25–28], in Fig. 9(a) we plot the penetration depth δ as a function of total drop distance $H = h + \delta$ for an impactor diameter of $D = 22.2$ mm. The plot shows that δ becomes smaller as the wet sand stiffens with the increase of S. We fit the data for five different ranges of S using a power-law function $\delta \propto (h + \delta)^{\alpha}$. We find that the power-law exponents have values that vary around $\alpha = 0.5$ (see the figure caption for details).

For a given impact energy, a smaller penetration depth results from a larger frictional resistance, which can be considered to be proportional to the yield stress, as discussed in Sec. II. Accordingly, we attempt to scale δ for targets with different S, using the yield stress [Fig. 1(b)]. In Fig. 9(b) we plot the dimensionless penetration depth δ/D as a function of

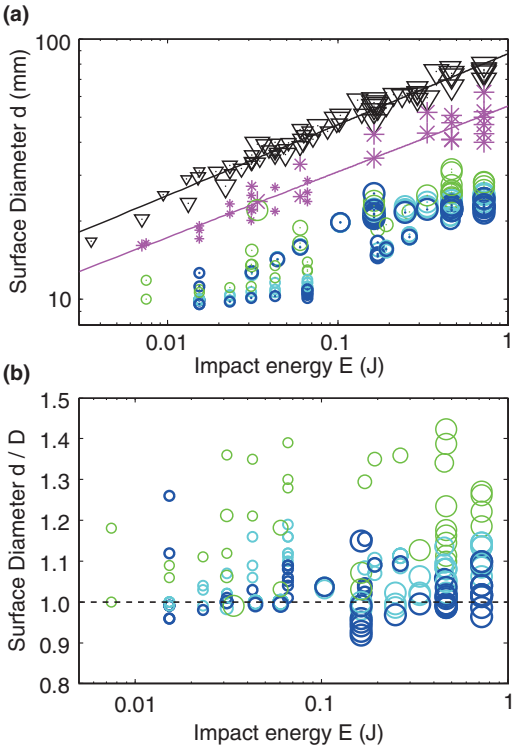

FIG. 7. (Color online) (a) Surface diameter d (mm) as a function of impact energy E (J) for different ranges of S. Marker sizes are proportional to the impactor diameter: inverted triangles, simple (here we plot the $S = 0$ cases only for simplicity); asterisks, transitional in the range of $0.024 \leqslant S \leqslant 0.037$; and circles, cylindrical in the range of $0.04 \leqslant S < 0.06$ (green, thin line), $0.06 \leqslant S < 0.15$ (light blue, medium line), and $0.15 \leqslant S < 0.6$ (blue, thick line). The power-law fits are given by $d = 87.5E^{0.271\pm0.007}$ (simple) and $d = 55.0E^{0.251\pm0.008}$ (transitional). The packing fraction for all data is $\phi = 0.517 \pm 0.011$. (b) Data for cylindrical craters in (a) replotted in terms of dimensionless surface diameter d/D for the vertical axis.

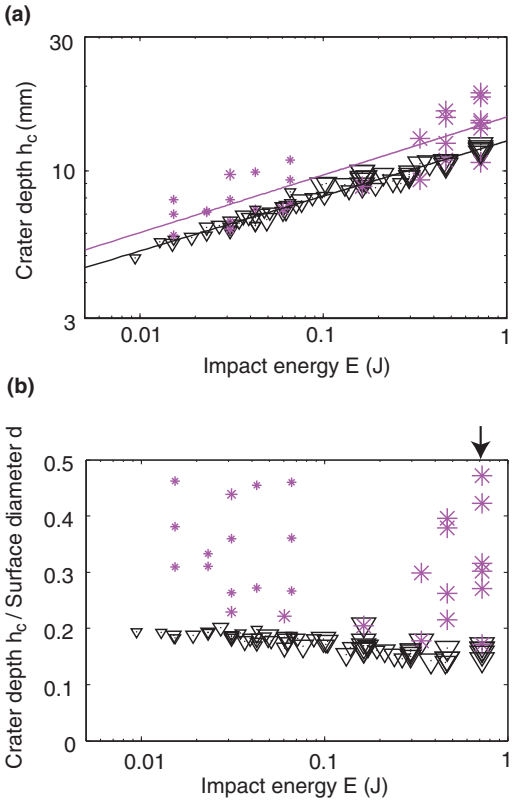

FIG. 8. (Color online) (a) Crater depth h_c (mm) as a function of impact energy E (J) at small S ($S < 0.04$) for the cases in which the impactor is fully submerged in the target. Marker sizes are proportional to the impactor diameter: inverted triangles, simple, for $S = 0$ only ($\phi = 0.526 \pm 0.003$); and asterisks, transitional in the range of $0.024 \leqslant S \leqslant 0.037$ ($\phi = 0.524 \pm 0.001$). Lines are power-law fits to the data: $h_c = 12.7E^{0.195\pm0.005}$ (simple) and $h_c = 15.5E^{0.206\pm0.013}$ (transitional). (b) Ratio h_c/d for the same data plotted in (a). The data points aligned vertically for an impact energy of $E = 0.73$ J (indicated by an arrow) correspond to those plotted in Fig. 6(d).

dimensionless inertia i' [Eq. (2)]. We find that δ/D for different S cases collapse fairly well. We fit the scaled result using a power-law function to obtain $\delta/D \propto i'^{0.517\pm0.011}$, indicating an exponent close to 0.5.

IV. DISCUSSION

A. Comparison with previous works

We now compare our scaling relations with those obtained from previous experiments. First we consider the results for dry granular matter. The power-law exponents of the diameter-energy relation for dry glass beads are $\simeq$0.25 [24,25,29]. Our results for dry sand is 0.271 ± 0.007 for surface diameters and 0.265 ± 0.006 for rim diameters, a slightly larger value but still close to 0.25. In contrast, the power-law exponents of the crater depth-energy relation for the dry glass beads is around 0.20 [30] and the ratio of the rim to floor depth to the rim diameter becomes smaller with impact energy [24]. Our experimental results are also in general agreement with these works.

Next we consider the relation of the penetration depth to the total drop distance for both the dry and wet granular matter targets. The power-law exponent α obtained from previous experiments using dry spherical glass bead targets has been somewhat variable, i.e., $\alpha = 0.33$ [10,12,25,27], 0.40 [18], and 0.4–0.6 [26]. Our obtained exponent of $\alpha \sim 0.44$ for $D = 22.2$ mm impactor penetrating into dry sand is within this range. de Bruyn and Walsh [26] showed that α becomes smaller with packing fraction ϕ. The $\phi \sim 0.5$ of our experiments is smaller than the $\phi \sim 0.6$ in most of the previous works. However, since we use aspherical sand rather than spherical beads used in previous works, a direct comparison is not possible. Marston *et al.* [10] obtained α for a wet granular matter (glass bead) target as $\alpha = 0.45$ and 0.55 for tapped and poured preparation cases respectively, values that are close to what we obtained. However, there are also several differences. First, their data show that α is larger for a wet granular target. Although our data shown in Fig. 9(a) also indicate an increase of α with S, the same trend is not found for an impactor diameter of $D = 10.0$ mm. Second, they report that under some conditions, δ of the wet target always exceeds that of the dry target, which we did not observe in our experiments.

We consider the reason for a power-law exponent α close to 0.5 for both dry and wet targets. Following Tsimring and Volfson [28], Katsuragi and Durian [12] showed

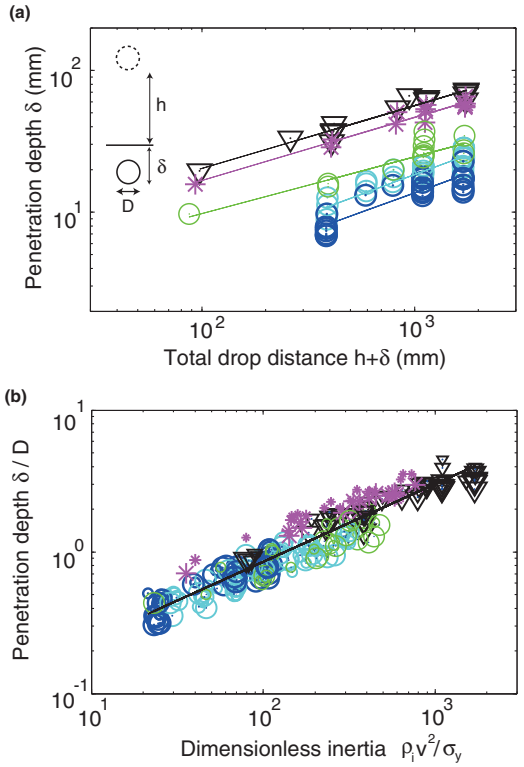

FIG. 9. (Color online) (a) Penetration depth δ (mm) as a function of total drop distance $H = h + \delta$ (mm) for $D = 22.2$ mm: inverted triangles, simple craters ($S = 0$ cases only), fitted as $\delta = 2.62H^{0.444\pm0.028}$; asterisks, transitional craters ($0.024 \leqslant S \leqslant 0.037$), fitted as $\delta = 2.16H^{0.445\pm0.031}$; and circles, cylindrical craters, fitted as $\delta = 1.53H^{0.402\pm0.053}$ [$0.04 \leqslant S < 0.06$ (green thin line)], $\delta = 0.40H^{0.553\pm0.051}$ [$0.06 \leqslant S < 0.15$ (light blue medium line)], and $\delta = 0.32H^{0.544\pm0.049}$ [$0.15 \leqslant S < 0.6$ (blue thick line)]. The packing fraction of the target is $\phi = 0.517 \pm 0.011$. (b) δ for different impactor diameters D and target water saturation plotted as a function of dimensionless inertia i' [Eq. (2)]. The data of (a) are included in the plot. σ_{y0} is obtained from the functional fit to the data shown in Fig. 1(b). Marker sizes are proportional to the impactor diameter. The line is a power-law fit to all data given by $\delta/D = 0.068i'^{0.548\pm0.012}$. The packing fraction is $\phi = 0.517 \pm 0.011$.

experimentally that both a Coulomb frictional drag $F(z)$, which increases with depth z as $\propto z$ [31–33], and an inertial drag, which increases with velocity v as $\propto v^2$, contribute to the drag. If we assume that a certain fraction f of the total impact energy is used against the frictional drag, the penetration depth δ is determined from the energy balance

$$\int_0^\delta F(z)dz = fmg(h+\delta) \equiv fE_p, \tag{3}$$

where E_p is the available potential energy. The above energy balance neglects the work done to excavate the crater (proportional to volume times the depth) E_x. We can estimate E_x for our experiments and indeed confirm that $E_x/E_p \sim 10^{-2} \ll 1$, a result that is consistent with that of previous work [30].

Here $F(z)$ may be expressed as $F(z) = \pi D^2 \sigma_y(z)$, where $\sigma_y(z)$ is the stopping stress as a function of depth. We show that a dependence $\sigma_y(z) = A\sigma_{y0}(z/D)$, where A is the scaling prefactor, explains our approximate scaling relation $\delta/D \propto (\rho v^2/\sigma_{y0})^{1/2}$, which is shown in Fig. 9(b). A similar derivation has been done previously [27]. The above expression indicates a frictional drag that increases with depth. In our experiments, because $\delta/h \leqslant 0.22$, we may approximate $h + \delta \sim h$. If we substitute these relations into Eq. (3), we obtain our approximate scaling relation. It also follows that if we use the prefactor of 0.068 in Fig. 9(b), we obtain $A/f \simeq 36$. Since we do not have measurements of the penetration depth versus time [12], we cannot obtain the individual values for f and A and discuss how they depend on other parameters. However, we can make order of magnitude estimates. Since σ_{y0} was measured at a depth $z \sim D$, we may estimate that $A \sim O(1)$. The ratio of frictional to inertial drag can be estimated as $1/i' \sim O(0.001\text{–}0.1)$, from which we obtain $f \sim O(0.001\text{–}0.1)$. Accordingly, $A/f \sim O(1\text{–}100)$, which is consistent with $A/f \simeq 36$ obtained from the fit.

Finally, we compare with previous experiments that indicate that changing parameters other than the saturation content S can also result in a similar change in crater shape. One is the particle size, which affects the target rheology because the cohesive stress scales inversely proportionally to the particle size. Indeed, Walsh *et al.* [24] showed that when the particle size of the glass beads is 0.045–0.090 mm, which is smaller than the particle size of the sand we used, the crater wall formed terraces and the crater diameter became smaller compared to the experiments with a target consisting of a larger particle size. They argue that one cause for the difference can be the particle cohesion arising from the air moisture [11]. The formation of terraces and the reduced crater diameter are similar to the transitional craters in our experiments. Another parameter is the packing fraction ϕ of the target. For a small ϕ, a porous target can be compacted and the ejecta dispersal be suppressed [34]. This is qualitatively similar to the cylindrical craters of our experiments.

B. Scaling to impact cratering in asteroids

Our low-velocity impact cratering experiments at $v = 1.2\text{–}5.8$ m/s correspond to the escape velocity of asteroids with a radius of the order of $R \sim 1$ km, which is among the smallest of the asteroids [35]. Here we attempt to scale our experiments to impact cratering with larger impactor size and smaller gravitational acceleration. We consider a self-gravitating spherical asteroid that consists of granular matter such as regoliths or rock fragments, which is indeed observed (see, e.g., [36]). In what follows we evaluate the dimensionless numbers i' and g' for an asteroid and evaluate the condition that corresponds to our experiments.

The yield stress of a granular target at a depth of δ may be estimated from the Coulomb's law

$$\sigma_y \sim \mu_{\rm eff}\rho_t g\delta. \tag{4}$$

Such a depth-strengthening property is confirmed from the penetrometer measurements into granular matter (see, e.g., [37,38]) and is analogous to the increase of frictional rock strength with depth (see, e.g., [39]) in the shallow parts of the Earth. As in our experiments, in what follows we consider a low-velocity impact in which the penetration depth scale of the impactor is comparable to the impactor size $\delta \sim D$ and, accordingly, $\sigma_y \sim \mu_{\rm eff}\rho_t g D$.

We consider an asteroid with a radius R. First we evaluate g' [Eq. (1)]. For a crater depth scale of the order of the impactor size D we obtain

$$g' = \frac{\rho_t g D}{\sigma_y} \sim \frac{1}{\mu_{\rm eff}}. \quad (5)$$

The exact value of $\mu_{\rm eff}$ is quite uncertain since it depends on various factors such as particle size, shape, and cohesion. Similar to our experiments, if there is an interstitial liquid or a volatile material [40], cohesion can become important. Even if such volatile materials are absent, the van der Waals cohesive force can become important for small particles [41]. Despite the uncertainty, we may assume $\mu_{\rm eff}$ of the order of 1–10 as obtained from our rheology measurements.

Next we evaluate i' [Eq. (2)]. A lower estimate for the impact velocity is the escape velocity v, which scales as $v \propto R\sqrt{\rho_t}$. The impact velocity can become faster if the impactor is being accelerated by nearby planets, or the sun. Gravitational acceleration scales as $g \propto \rho_t R$ and, accordingly, i' becomes

$$i' = \frac{\rho_i v^2}{\sigma_y} = \left(\frac{1}{\mu_{\rm eff}}\right)\left(\frac{\rho_i}{\rho_t}\right)\left(\frac{2R}{D}\right). \quad (6)$$

Here we attempt to evaluate quantitatively. According to Eq. (5), g' is determined only by the target friction $\mu_{\rm eff}$ and becomes of the order of $g' = 0.01-0.1$. This overlaps our experimental range of $0.05 < g' < 2$, which covers the transition between the strength and gravity regimes. Next we consider the situation for our experimental ranges of $20 < i' < 2000$ under which the assumption of $\delta \sim D$ is valid. Assuming $\rho_i \sim \rho_t$ and $\mu_{\rm eff} \sim 10$, from Eq. (6), our experimental i' range corresponds to the situation for $10^{-4} < D/R < 10^{-2}$. If we consider an asteroid $R_p \sim 1$ km, our experimental range of i' corresponds to an impactor with a size of $D \sim 0.1$–10 m. Although the above estimates are crude, we can expect that similar granular impact cratering may occur in small asteroids. In addition, because g' is of the order of 0.01–0.1, we expect diverse crater shapes to form.

V. CONCLUSION

A series of low-velocity impact cratering experiments in a wet sand target was conducted by carefully controlling the water saturation S. We find that diverse crater shapes form as we increase S in small increments. The presence of a small amount of interstitial water ($S < 0.04$) strongly inhibits the crater wall collapse. This results in the steepening of the crater wall and the decrease of the crater diameter. For $0.04 < S < 0.65$ the wet sand becomes sufficiently stiff that a cylindrical crater forms, whereas for $S > 0.65$, the wet sand becomes fluidized such that the crater diameter and depth increase. Additional experiments with different impactor size and release heights showed that for a dry and slightly wet ($S < 0.02$) sand target, the crater diameter scales well with the gravity regime scaling. However, the scaling fails as we increase S and the wet sand stiffens. In contrast, the impactor penetration depth was found to scale proportionally to $(\sigma_i/\sigma_{y0})^{1/2}$ (where σ_i denotes the inertial stress) for targets with a wide range of S. These differences in scaling are interpreted as arising from d being affected by the cease of crater wall collapse as S is increased, whereas δ remains relatively unaffected by whether or not the collapse occurs because penetration occurs prior to collapse.

ACKNOWLEDGMENTS

We thank F. Shibuya for devising the method for wet sand preparation [17]; N. Endo, K. Kashiwaya, and A. Namiki for technical support; and the two anonymous reviewers for helpful comments on the manuscript. This work was supported by KAKENHI Grants No. 21654068, No. 22109505, and No. 24244073.

[1] S. Herminghaus, Adv. Phys. **54**, 221 (2005).
[2] N. Mitarai and F. Nori, Adv. Phys. **55**, 1 (2006).
[3] S. Nowak, A. Samadani, and A. Kudrolli, Nat. Phys. **1**, 50 (2005).
[4] M. Scheel, R. Seemann, M. Brinkmann, M. D. Michiel, B. Breidenbach, and S. Herminghaus, Nat. Mater. **7**, 189 (2008).
[5] M. Pakpour, M. Habibi, P. Moller, and D. Bonn, Sci. Rep. **2**, 549 (2012).
[6] D. E. Gault and R. Greely, Icarus **34**, 486 (1978).
[7] J. H. Fink, R. Greely, and D. E. Gault, Proc. Lunar Planet. Sci. B **12**, 1649 (1981).
[8] K. A. Holsapple, Annu. Rev. Earth Planet. Sci. **21**, 333 (1993).
[9] M. Manga, A. Patel, J. Dufek, and E. S. Kite, Geophys. Res. Lett. **39**, L050192 (2012).
[10] J. O. Marston, I. U. Vakarelski, and S. T. Thoroddsen, Phys. Rev. E **86**, 020301 (2012).
[11] J. Duran, *Sands, Powders, and Grains, An Introduction to the Physics of Granular Materials* (Springer, New York, 2000).
[12] H. Katsuragi and D. J. Durian, Nat. Phys. **3**, 420 (2007).
[13] T. M. G. Mavko and J. Dvorkin, *The Rock Physics Handbook* (Cambridge University Press, Cambridge, 1998).
[14] D. J. Hornbaker, R. Albert, I. Albert, A.-L. Barabaśi, and P. Schiffer, Nature (London) **387**, 765 (1997).
[15] N. J. Alderman, G. H. Meeten, and J. D. Sherwood, J. Non-Newtonian Fluid Mech. **39**, 291 (1991).
[16] I. Sumita and Y. Ota, Earth Planet. Sci. Lett. **304**, 337 (2011).
[17] F. Shibuya, M.S. thesis, Kanazawa University, 2010.
[18] A. Seguin, Y. Bertho, and P. Gondret, Phys. Rev. E **78**, 010301 (2008).
[19] K. A. Holsapple and R. M. Schmidt, *Proceedings of the Tenth Lunar and Planetary Science Conference* (Pergamon, New York, 1979), p. 2757.
[20] M. Arakawa and M. Yasui, Icarus **216**, 1 (2011).
[21] A. Suzuki, S. Hakura, T. Hamura, M. Hattori, R. Hayama, T. Ikeda, H. Kusuno, H. Kuwahara, Y. Muto, K. Nagaki, R. Niimi, Y. Ogata, T. Okamoto, T. Sasamori, C. Sekigawa, T. Yoshihara, S. Hasegawa, K. Kurosawa, T. Kadono, A. M. Nakamura, S. Sugita, and M. Arakawa, J. Geophys. Res. **117**, E08012 (2012).
[22] See Supplemental Material at http://link.aps.org/supplemental/10.1103/PhysRevE.88.022203 for movies of the experiments.

[23] M. P. Ciamarra, A. H. Lara, A. T. Lee, D. I. Goldman, I. Vishik, and H. L. Swinney, Phys. Rev. Lett. **92**, 194301 (2004).
[24] A. M. Walsh, K. E. Holloway, P. Habdas, and J. R. de Bruyn, Phys. Rev. Lett. **91**, 104301 (2003).
[25] J. S. Uehara, M. A. Ambroso, R. P. Ojha, and D. J. Durian, Phys. Rev. Lett. **90**, 194301 (2003).
[26] J. R. de Bruyn and A. M. Walsh, Can. J. Phys. **82**, 439 (2004).
[27] M. A. Ambroso, C. R. Santore, A. R. Abate, and D. J. Durian, Phys. Rev. E **71**, 051305 (2005).
[28] L. S. Tsimring and D. Volfson, in *Powders and Grains 2005*, edited by R. Garcia-Rojo, H. J. Herrmann, and S. McNamara (Balkema, Rotterdam, 2005), pp. 1215–1223.
[29] J. C. Amato and R. E. Williams, Am. J. Phys. **66**, 141 (1998).
[30] S. J. de Vet and J. R. de Bruyn, Phys. Rev. E **76**, 041306 (2007).
[31] D. Lohse, R. Rauhé, R. Bergmann, and D. van der Meer, Nature (London) **432**, 689 (2004).
[32] M. A. Ambroso, R. D. Kamien, and D. J. Durian, Phys. Rev. E **72**, 041305 (2005).
[33] M. Hou, Z. Peng, R. Liu, K. Lu, and C. K. Chan, Phys. Rev. E **72**, 062301 (2005).
[34] K. R. Housen, K. A. Holsapple, and M. E. Voss, Nature (London) **402**, 155 (1999).
[35] E. Asphaug, Annu. Rev. Earth Planet. Sci. **37**, 413 (2009).
[36] A. Fujiwara, J. Kawaguchi, D. K. Yeomans, M. Abe, T. Mukai, T. Okada, J. Saito, H. Yano, M. Yoshikawa, D. J. Scheeres, O. Barnouin-Jha, A. F. Cheng, H. Demura, R. W. Gaskell, N. Hirata, H. Ikeda, T. Kominato, H. Miyamoto, A. M. Nakamura, R. Nakamura, S. Sasaki, and K. Uesugi, Science **312**, 1330 (2006).
[37] H. Mizutani, S.-I. Kawakami, Y. Takagi, M. Kato, and M. Kumazawa, J. Geophys. Res. **88**, 835 (1983).
[38] M. B. Stone, R. Barry, D. P. Bernstein, M. D. Pelc, Y. K. Tsui, and P. Schiffer, Phys. Rev. E **70**, 041301 (2004).
[39] D. L. Turcotte and G. Schubert, *Geodynamics* (Cambridge University Press, Cambridge, 2002).
[40] E. Asphaug, in *Asteroids III*, edited by J. W. F. Bottke, A. Cellino, P. Paolicchi, and R. P. Binzel (University of Arizona Press, Tucson, 2002), pp. 463–484.
[41] D. J. Scheeres, C. M. Hartzell, P. Sańchez, and M. Swift, Icarus **210**, 968 (2010).